Journal of Molecular Catalysis A: Chemical 298 (2009) 40–50

Contents lists available at ScienceDirect

Journal of Molecular Catalysis A: Chemical

journal homepage: www.elsevier.com/locate/molcata

Effect of the silica texture on the structure of supported metallocene catalysts

Fernando Silveira[a], Maria do Carmo Martins Alves[a], Fernanda C. Stedile[a], Sibele B. Pergher[b], Arnaud Rigacci[c], João Henrique Zimnoch dos Santos[a,*]

[a] Instituto de Química, UFRGS, Av. Bento Gonçalves, 9500 – Porto Alegre - 91509-900, Brazil
[b] Departamento de Química, URI - Campus Erechim, CP 743, Erechim 99700-000, Brazil
[c] École des Mines de Paris, Center for Energy and Processes (CENERG), BP 207, F-06904 Sophia, Antipolis Cedex, France

ARTICLE INFO

Article history:
Received 29 August 2008
Accepted 7 October 2008
Available online 17 October 2008

Keywords:
Supported metallocene
MALDI-TOF-MS
EXAFS
AFM
Chrysotile

ABSTRACT

A series of hybrid supported catalysts was prepared by sequentially grafting Cp_2ZrCl_2 and $(n\text{BuCp})_2ZrCl_2$ (1:3 ratio) onto synthesized xerogel, aerogel, commercial silicas, MCM-41 and leached chrysotile. The supported catalysts were characterized by Rutherford backscattering spectrometry, matrix assisted laser desorption ionization time of flight mass spectroscopy, atomic force microscopy, extended X-ray absorption fine structure spectroscopy and nitrogen adsorption. The grafted metal content was between 0.15 and 0.84 wt.% Zr/SiO_2. All the systems were shown to be active in ethylene polymerization with methylaluminoxane as the cocatalyst. The catalyst activity and molecular weight were shown to depend on the effect impinged by the textural characteristic of the supports on the structure of the supported catalyst species. The highest activity in ethylene polymerization (ca. 5300 kgPE $molZr^{-1}$ h^{-1}) was reached with the supported catalyst using commercial silicas with narrow pore diameter and volume distribution. Polymers with higher molecular weight, characterized by gel permeation chromatography and differential scanning calorimetry, were associated with the reduction in the interatomic Zr–O distance, which was shown to be dependent on the support properties.

1. Introduction

Supported metallocenes have been investigated in the last 20 years. Many routes of immobilization have been proposed, affording different catalyst activity or polymer properties [1]. The performance of an immobilized metallocene may be changed in comparison to the homogeneous counterpart due to electronic and steric effects attributed to the support. Most of the supported metallocenes have exhibited lower catalytic activities. Furthermore, polymer properties usually differ from those produced with the homogeneous complexes [1–3]. According to the literature, the reduction in catalytic activity has been attributed to: (i) deactivation of the metallocene complexes during the grafting reaction, (ii) inaccessibility of the metallocene complexes to the cocatalyst (methylaluminoxane, MAO) hindering its activation, (iii) generation of active sites with lower propagation rates due to interactions with the support surface, and (iv) restrictions of the monomer access to the active sites hindering the chain propagation [4]. Generally, polymers produced with supported metallocenes have a higher average molecular weight due to a reduction in the rate of termination reactions [4–7]. Conversely, polymers with lower crystalline fractions have been produced with supported metallocene [8]. Changes in the stereoregularity and stereospecificity of the active sites generated by supporting a metallocene have also been reported [1]. Furthermore, a decrease in the insertion of long chain branches for supported metallocenes has been observed [5–7].

In spite of having been investigated for a long time, the field of supported metallocenes still attracts much attention. Silica has been the most investigated and proposed support. Recent research has dealt with other alternatives such as: the development of supported catalysts on tubular mesoporous aluminas capable of producing polyethylene nano-fibers [9], immobilization on nanosilicas [10], aluminophosphinates [11] and polymers [12], metallocenes encapsulated on silica produced by sol–gel [13], grafting on sulphonic-acid modified SBA [14] or $MgCl_2$-based supports [15], to mention a few. Such examples suggest that the support may play an important role in the development of a supported catalyst.

In previous work, we reported the effect of grafting Cp_2ZrCl_2 and $(n\text{BuCp})_2ZrCl_2$ on the same support (silica), at different order and molecular ratios, on the catalyst activity and on the polymer properties. The best catalyst system was that resulting from grafting Cp_2ZrCl_2 followed by $(n\text{BuCp})_2ZrCl_2$ in a 1:3 ratio [16,17]. In a subsequent paper, both catalysts were grafted on silica supports

* Corresponding author. Tel.: +55 51 3308 7238; fax: +55 51 3308 7304.
E-mail address: jhzds@iq.ufrgs.br (J.H.Z.d. Santos).

1381-1169/$ – see front matter © 2008 Elsevier B.V. All rights reserved.
doi:10.1016/j.molcata.2008.10.011

produced by sol–gel (xerogel and aerogel) and precipitation methods. The catalyst activity and molecular weight were shown to depend on the textural characteristic of the silicas, namely grain size and pore diameter [18].

In the present study, we comparatively investigated the effect of the microstructure of different silica-based supports on the structure of the resulting grafted metallocene species. Different silica supports were employed: amorphous (commercial silicas, synthesized xerogel and aerogel silicas), crystalline (silica MCM-41) and fiber-like (from leached chrysotile) silicas. Cp_2ZrCl_2 and $(n\text{BuCp})_2ZrCl_2$ were grafted onto the supports in a 1:3 ratio. The resulting catalysts were characterized by Rutherford backscattering spectrometry (RBS), matrix assisted laser desorption ionization time of flight mass spectroscopy (MALDI-TOF-MS), atomic force microscopy (AFM), extended X-ray absorption structure (EXAFS) spectroscopy and nitrogen adsorption. The hybrid-supported catalysts were evaluated in ethylene polymerization with MAO as the cocatalyst. The polymers were characterized by gel permeation chromatography (GPC) and differential scanning calorimetry (DSC).

2. Experimental

2.1. Materials

All chemicals were manipulated under inert atmosphere using the Schlenk technique. All supports were activated under vacuum ($P < 10^{-5}$ bar) for 16 h at 450 °C. $(n\text{BuCp})_2ZrCl_2$ (Aldrich), Cp_2ZrCl_2 (Aldrich), $Si(OEt)_4$ (Merck), $SiCl_4$ (Merck), $ZrCl_4$ (Aldrich) and MAO (Witco, 10.0 wt.% toluene solution) were used without further purification. Ethylene and argon (White Martins) were passed through a molecular sieve (13 Å) prior to use. Toluene was purified by refluxing with sodium, followed by distillation under nitrogen just before use.

2.2. Preparation of the silica-based supports

2.2.1. Synthesis of xerogel silica by the hydrolytic acid route [19–20]

Tetraethylorthosilicate ($Si(OEt)_4$) and HNO_3 (0.3 M) were poured together into a glass reactor and vigorously stirred at room temperature. The H_2O:$Si(OEt)_4$ volume ratio was kept under 2. Initially, the mixture was separated into two phases. When the mixture was stirred, an emulsion was formed and water was dispersed as droplets. After 3–10 min, a homogeneous solution was formed. In the following days, the viscosity increased and a solid transparent monolith was obtained. The resulting xerogel (6.30 g) was washed with acetone and dried at 140 °C for three days.

2.2.2. Synthesis of aerogel silica

Aerogel silica was synthesized by the sol–gel method under supercritical conditions at CENERG (France). The experimental conditions are described elsewhere [21].

2.2.3. Chrysotile leaching

Natural chrysotile (ca. 30 g) was mixed with (1 L) of a hydrochloric acid solution (5.0 mol L^{-1}), according to the leaching procedure described in literature [22]. This suspension was stirred for 48 h at 626 °C yielding 15.0 g of product. The resulting leached chrysotile was abundantly washed with deionized water and dried.

2.3. Synthesis of supported hybrid catalysts

A Cp_2ZrCl_2 toluene solution corresponding to 0.25 wt.% Zr/SiO_2 was added to ca. 1.0 g of pre-activated silica and stirred for 30 min at room temperature. The solvent was removed under vacuum through a fritted disk. A $(n\text{BuCp})_2ZrCl_2$ toluene solution corresponding to 0.75 wt.% Zr/SiO_2 was added and the resulting slurry was stirred for 30 min at room temperature, and then filtered through a fritted disk. The resulting solids were washed with $15 \times 2.0\ cm^3$ of toluene and dried under vacuum for 4 h.

The procedure above was used for all of the silicas used in this work (Grace 956, 955 and 948, xerogel silica by the hydrolytic route and aerogel silica, MCM-41, and leached Chrysotile). These silicas generated the heterogeneous catalytic systems after grafting, respectively: G56, G55, G48, HYD, AER, M41 and lCR.

2.4. Characterization of supported catalysts

2.4.1. Rutherford backscattering spectrometry (RBS)

The zirconium loadings in the catalysts were determined by RBS, using He^+ beams of 2.0 MeV incidence, on homogeneous tablets of the compressed (12 MPa) powder of the catalyst systems. The method is based on the determination of the number and energy of the detected particles which are elastically scattered in the Coulombic field of the atomic nuclei in the target. In this study, the Zr/Si atomic ratio was determined by the heights of the signals corresponding to each of the elements in the spectra and converted to wt.% Zr/SiO_2. For an introduction to the method and applications of this technique the reader is referred elsewhere [23].

2.4.2. Fourier transform infrared spectroscopy (FT-IR)

Samples were analyzed as pellets, diluted in KBr, by absorbance FTIR, using a BOMEM FTIR spectrophotometer (MB-102) at 25 °C by coadding 32 scans at a resolution of 4 cm^{-1}. The measurements were restricted to the 4000–2500 cm^{-1} region.

2.4.3. Nitrogen adsorption–desorption isotherms

Samples were previously degassed (10^{-2} mbar) at 120 °C (silica) or at 85 °C (supported catalysts) for 8 h. Adsorption–desorption nitrogen isotherms were measured at −196 °C in a Gemini 2375 (Micromeritics). Specific surface areas (S_{BET}) were determined by the Brunauer–Emmett–Teller equation ($P/P_0 = 0.05$–0.35). The mesopore size and distribution were calculated by the Barrett–Joyner–Halenda (BJH method) using the Halsey standards. Desorption branch was used.

2.4.4. Atomic force microscopy (AFM)

Images of silica and supported catalyst surfaces were obtained using an atomic force microscope, Nanoscope IIIa®, manufactured by Digital Instruments Co., using the contact mode technique with probes of silicon nitride. WS M 4.0 software from Nanotec Electronic S.L. [24] was used for the image treatment. Samples were compressed in the form of tablets and fragments of roughly 16 mm^2 which were employed for the analysis.

2.4.5. Extended X-ray absorption fine structure (EXAFS)

EXAFS measurements were performed around the Zr K edge ($E = 17{,}998$ eV) using the Si(2 2 0) channel-cut monochromator at the XAFS 1 beamline (LNLS, Campinas, Brazil). The spectra were collected in the fluorescence mode using one ionization chamber filled with argon and a Si(Li) detector. In order to perform EXAFS experiments, the powder of the supported metallocenes was compacted into a pellet and covered with Kapton® tape. All the manipulations were performed in a dry box to avoid the occurrence of oxidation reactions. The EXAFS spectra were acquired from 17,900 up to 18,900 eV with a 3 eV step. Several scans were averaged in order to improve the signal to noise ratio.

The lFEFFIT analysis package [25] and the Winxas program [26] were used for the EXAFS data analysis. The EXAFS signal between 1.0 and 10.0 $Å^{-1}$ was Fourier-transformed with a k^1 weighting and

a Bessel window. Structural parameters were obtained from a least squares fitting in k and R space using theoretical phase shift and amplitude functions deduced from the FEFF7 code [25]. The input for the FEFF7 code was provided by the ATOMS program [27]. In the fitting procedure, the amplitude reduction factor ($S_0{}^2$) was close to 1.0 for all samples, and the threshold energy (E_0) was −7.5 eV for the Zr–C pair and −3.5 eV for the Zr–O pair.

2.4.6. Matrix assisted laser desorption ionization time of flight mass spectroscopy (MALDI-TOF-MS)

Measurements were performed in a MALDI Q-Tof Premier mass spectrometer (Waters Inc.), using a Nd:YAG (355 nm) laser operating at 200 Hz. Samples were prepared as a slurry and deposited on a spotter in triplicate. A spectral calibration was carried out using polyethylene glycol in the 400–3000 m/z range. The collision energy was 10 eV and the laser energy 200 a.u. A series of matrixes were employed. Nevertheless, as reported in literature [28], a better characterization was achieved in the absence of a matrix due to the existence of the strong chromophore groups already present in the metallocenes [29].

2.5. Polymerization reactions

Polymerizations were performed in toluene (0.15 L) in a 0.30 L Pyrex glass reactor connected to a constant temperature circulator equipped with mechanical stirring and inlets for argon and monomers. For each experiment, a mass of the catalyst system corresponding to 10^{-5} mol L^{-1} of Zr was suspended in 0.01 L of toluene and transferred into the reactor under argon. The polymerizations were performed at the atmospheric pressure of ethylene at 60 °C for 30 min at Al/Zr = 1000, using MAO as the cocatalyst. Acidified (HCl) ethanol was used to quench the processes, and the reaction products were separated by filtration, washed with distilled water, and finally dried under reduced pressure at 60 °C.

2.6. Polyethylene characterization

Molar masses and molar mass distributions were investigated with a Waters CV plus 150C high-temperature GPC instrument, equipped with a viscosimetrical detector, and three Styragel HT type columns (HT3, HT4 and HT6) with an exclusion limit of 1×10^7 for polystyrene. 1,2,4-Trichlorobenzene was used as the solvent, at a flow rate of 1 cm^3 min^{-1}. The analyses were performed at 140 °C. The columns were calibrated with standard narrow molar mass distribution polystyrenes and with linear low density polyethylenes and polypropylenes.

Polymer melting points (T_m) and crystallinities (χ_c) were determined on a TA Instrument DSC 2920 differential scanning calorimeter connected to a thermal analyst 5000 integrator and calibrated with indium, using a heating rate of 20 °C min^{-1} in the temperature range of 30–150 °C. The heating cycle was performed twice, but only the results of the second scan are reported, because the former is influenced by the mechanical and thermal history of the samples. SEM experiments were carried on a JEOL JSM/6060. The powder was initially fixed on a carbon tape and then coated with gold by conventional sputtering techniques. Powder X-ray diffraction analysis was accomplished in a DIFFRAKTOMETER model D5000 (Siemens) using a Ni filter and CuKα (λ = 1.54 Å) radiation.

3. Results and discussion

The silica surface, at least for moderate activation temperatures, is mainly composed of isolated and, to a lesser extent, vicinal and geminal hydroxyl groups, as well as relatively unreactive siloxane bridges [30]. Silanol groups are capable of reacting with sequestering agents such as organometallic chlorides and alkoxides, with the elimination of one or more of the original ligands. In the present case, zirconocenes are grafted on the silica surface by elimination of the chloride ligand with hydrogen atoms from the silanol groups, leading to the formation of surface species.

Table 1 shows the resulting grafted metal content (determined by RBS), specific area and pore diameter (calculated from the BET method) and catalyst activity in ethylene polymerization for the different supported systems.

According to Table 1, the grafted metal content lain between 0.15 and 0.84 wt.% Zr/SiO_2. Grafted metal contents around 0.40 wt.% Zr/SiO_2 have been reported in literature in the case of silica as a support [3].

The specific surface area of the supported catalysts was determined by nitrogen adsorption (Table 1). The catalysts, employing the three commercial silicas as supports, presented a surface area in the range of 200–250 m^2 g^{-1}. The catalyst employing a xerogel prepared by the hydrolytic route afforded a supported zirconocene catalyst bearing 341 m^2 g^{-1}. Catalysts generated on Aerogel and MCM-41 present a typical high specific area intrinsic to these kind of materials, which are dried under supercritical conditions and synthesized using a template, respectively [31,32]. The use of leached chrysotile (submitted to acid washing, which allows us to remove brucite from the external surface [33]) led to the synthesis of a supported catalyst with a specific area of approximately 226 m^2 g^{-1}.

The supported catalysts were further characterized by EXAFS in order to measure the interatomic distance of the constituents of these supported catalysts. The Fourier transforms shown in Fig. 1 display the main peaks centered at approximately 1.4 Å for all samples, which is extended roughly up to 2 Å.

The ratio of the spectra did not allow us to fit structural parameters beyond two shells: the Zr–C and Zr–O pairs. All the peaks following the first one are affected by noise, and therefore cannot be considered as real or acutely interatomic in these systems. Similar data treatments were performed by Mäkelä-Vaarne et al. [34] and Jezequel et al. [35] for a silica-supported zirconocene and hafnocene, respectively. In the present study, there was a lack of reproduction in the coordination number (N) and Debye–Waller factor (σ^2) values, rendering any assertion about these two

Table 1
Grafted metal content, textural characteristics and catalyst activity in ethylene polymerization of the different supported systems.

Catalysts	Zr/SiO_2 (wt.%)	Specific surface area (m^2 g^{-1})	Pore diameter (Å)	Catalytic activity (kgPE molZr^{-1} h^{-1})
G56	0.51	200 ± 3	145	4280
G55	0.33	244 ± 2	128	2220
G48	0.35	249 ± 3	118	5310
HYD	0.50	341 ± 0	39	1680
AER	0.15	462 ± 2	58	3537
M41	0.84	768 ± 1	24	1927
ICR	0.20	226 ± 0	39	880

[Zr] = 10^{-5} mol L^{-1}; [Al/Zr] = 1000; V = 0.15 L (toluene); P = 1 bar (ethylene); T = 60 °C; t = 30 min.

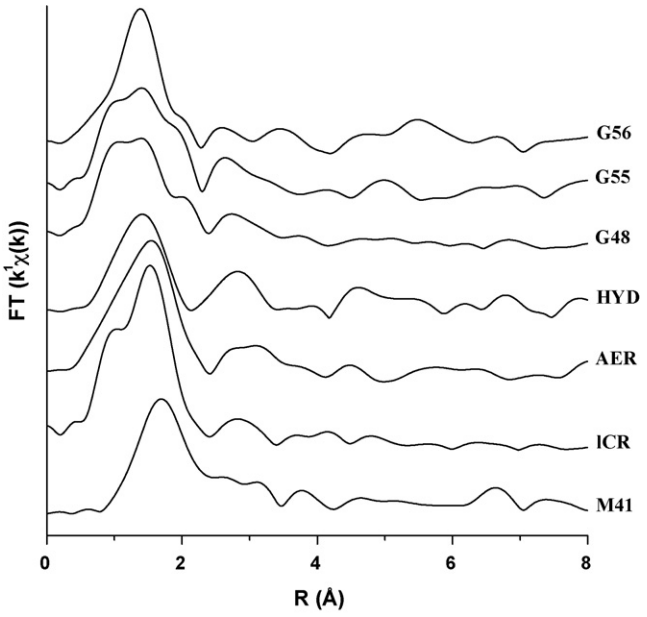

Fig. 1. Fourier transform of the EXAFS signal.

parameters imprecise, since they are highly correlated. Therefore, we opted for structural analysis taking into account only the interatomic (R) distances shown in Table 2. For comparative reasons, data from the homogeneous complexes were also included.

The results have shown that Zr–C interatomic distances vary between 1.5 and 2.2 Å, i.e., there is a reduction in the Zr–C interatomic distance for the supported metallocenes in comparison to the homogeneous catalysts, which were 2.34 and 2.35 Å, respectively, for Cp_2ZrCl_2 and $(n\text{BuCp})_2ZrCl_2$.

According to Fig. 2, an increase in support pore diameter seems to engender a reduction in the Zr–C interatomic distance. The lCr supported catalyst does not follow this trend, probably due to its pore shapes, which are formed from slits between the fibers [33].

Table 2
EXAFS parameters obtained through the first FT peak fit. R is the interatomic distance and χ^2 is the fit quality.

Catalysts	Bond χ^2	Distance R (Å)	
G56	Zr–C	1.50 ± 0.02	0.8
	Zr–O	2.02 ± 0.02	
G55	Zr–C	1.92 ± 0.02	0.8
	Zr–O	2.07 ± 0.02	
G48	Zr–C	1.95 ± 0.02	0.7
	Zr–O	2.09 ± 0.02	
HYD	Zr–C	2.17 ± 0.02	0.9
	Zr–O	1.98 ± 0.02	
AER	Zr–C	2.00 ± 0.02	0.4
	Zr–O	2.14 ± 0.02	
M41	Zr–C	2.20 ± 0.02	1.2
	Zr–O	2.05 ± 0.02	
lCR	Zr–C	1.86 ± 0.02	0.5
	Zr–O	2.05 ± 0.02	
Cp_2ZrCl_2	Zr–C	2.34 ± 0.02	
	0.5		
$(n\text{BuCp})_2ZrCl_2$	Zr–C	2.35 ± 0.02	
	0.4		

E_0 = Zr–C: −7.5 eV and Zr–O: −3.5 eV.

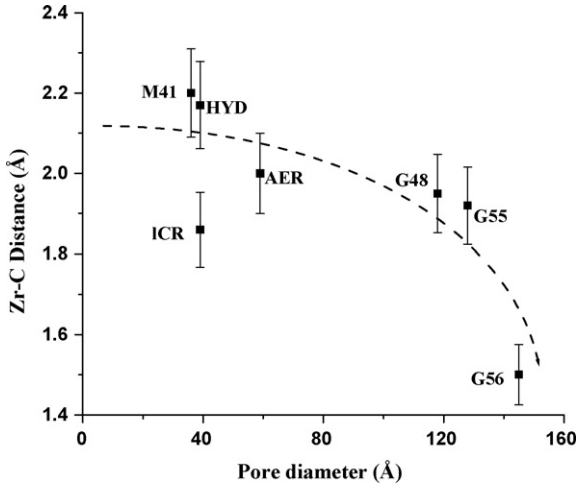

Fig. 2. Relationship between the Zr–C interatomic distance and the support pore diameter.

The results shown in Fig. 2 may suggest that the grafted metallocenes within the pores are somehow interacting with the pore walls, which may contribute to the variations observed in the Zr–C interatomic distances. The effect caused by the pore surface may be engendered by the residual silanol groups which remain inside the pores. In the case of small pores, the proximity between silanol groups and the metallocenes may cause an interaction, provoking an increase in the Zr–C distance.

In order to investigate the presence of intra-globular silanol groups, which absorb near 3650 cm^{-1} [30], transmission infrared spectra were recorded for the supported catalysts. Fig. 3 shows the resulting FT IR spectra of G56 and M41.

According to Fig. 3, there are residual intra-globular silanol groups: a higher number of intra-globular silanols was observed in the case of M41, in comparison to that of G56. One can presume that smaller pores are more likely to bear a higher amount of residual silanol groups, which were not consumed during the grafting reaction. Then, the higher number of silanol groups allied to the higher proximity between them and the grafted zirconocene species, due to the narrower pore diameter, might engender an increasing in the Zr–C distance, as depicted in Scheme 1.

These results are in agreement with Iler [36], who observed that for a pore diameter narrower than 100 Å, the negative curve of the

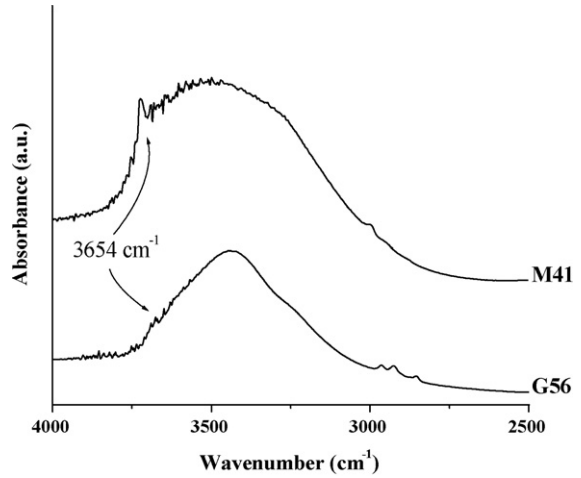

Fig. 3. Infrared spectra of G56 e M41.

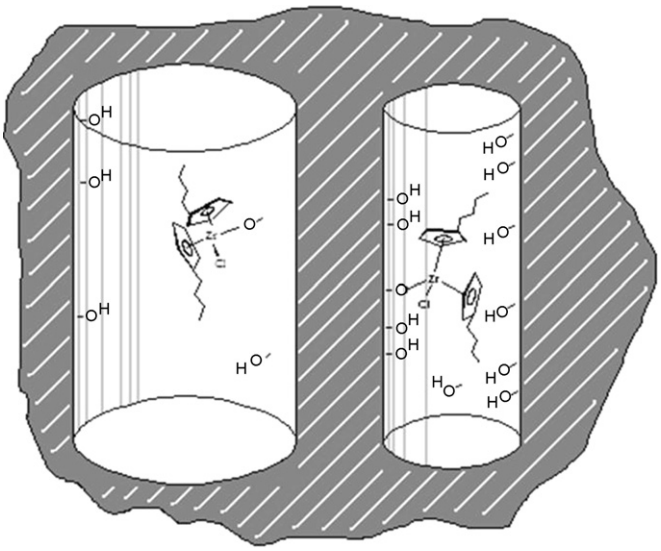

Scheme 1. Broad (**I**) and narrow (**II**) pore diameter with intra-globular silanol groups.

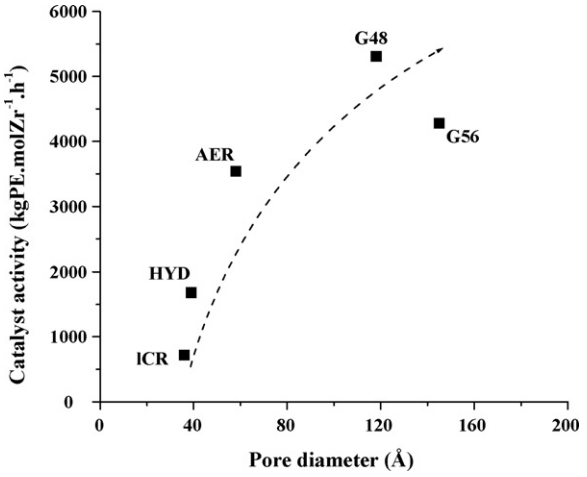

Fig. 4. Relationship between the support pore diameter and the catalytic activity in ethylene polymerization.

pore surface engenders an approximation among silanol groups, favoring the formation of hydrogen bonding, which in turn affords an enhancement in the stability of such silanol groups: dehydroxylation reactions turn more difficult, affecting the population of residual silanol groups.

3.1. Catalyst activity in ethylene polymerization

The proximity among silanol groups (vicinal silanols) can promote the generation of bidentate species, which are known to be inactive in polymerization. Such a phenomenon was already investigated taking into account the thermal treatment of silica (and therefore, the silanol group density): a lower thermal temperature engendered a higher number of silanol groups, higher grafted zirconocene content, but lower catalyst activity [37]. Legrand et al. [38] mentioned that supports treated at lower temperature (therefore, with a larger number of silanol groups) afforded higher grafted metal content, but the resulting supported metallocenes were shown to be less active in ethylene polymerization.

According to Table 1, catalysts HID, AER, M41 and lCR present pore diameters lower than 100 Å. The high metal content detected in HYD and M41 might have generated bidentate species. This fact could explain the low activity exhibited by such catalysts systems in comparison to that observed in the case of AER which, in spite of bearing very low grafted zirconocene content (0.15 wt.% Zr/SiO_2), has a relatively high catalyst activity.

Fig. 4 shows the relationship between catalyst activity and pore diameter.

According to Fig. 4, the catalyst activity increases as the pore diameter is enhanced. A similar effect has been reported by Pullukat [39], who observed that the broader the silica pore diameter, the higher the catalyst activity exhibited by silica-grafted $(n\text{BuCp})_2ZrCl_2$.

Silicas with a pore diameter in the range of 50–200 Å are usually preferred in the preparation of industrial applications [40]. For our supported catalysts, the BET method allowed us to calculate the pore size distribution in the micropore (pore diameter up to 20 Å) and mesopore (pore diameter between 20 and 500 Å) ranges. Then, the analysis of pore size distribution of the supported catalyst might provide some insight of their effect on the catalyst activity.

The mean pore size distribution curves of the supported catalysts expressed in terms of pore area and pore volume are shown in Fig. 5. For every curve, the presence of two regions can be observed: one of pore diameter in the range of 10–40 Å (micropores) and another for values higher than 45 or 80 Å. The latter shows a broadening in the pore size distribution, due to the increase in diameter and area of such pores. For G48, G56, G55 and AER, the pore size distribution is around 50 and 160 Å; for M41, HYD and lCR about 17 and 65 Å.

The curves were integrated between the range from 13 to 50 Å and from 51 to 180 Å, in order to get the percentage of the micropore area. Concerning the silica bearing the lowest fraction of micropore, the commercial silica exhibited a clear relationship between the fraction of micropore and catalyst activity. These results are in agreement with those observed by McDaniel [41], that evaluated several silica bearing similar specific area, but differing in the distribution of pore size and concluded that the increase in catalyst activity was accompanied by the reduction of the fraction of micropore (pore diameter lower than 100 Å). In other words, a higher amount of small pores renders the surface discontinuous, creating obstacles caused by the reduction of the wall thickness of these pores. In this case, this surface plays the role of an obstacle for the catalyst, cocatalyst and monomer. Stoiljkovic et al. [42] simulated the creation of obstacles on a silica surface, while varying the fraction of micropores, and evaluated their effect on the amount of active catalytic sites. The authors concluded that the increase of obstacles reduces catalyst activity, analogous to what is observed in the present study, in which an increase in the fraction of micropores among the evaluated commercial silicas engenders a decrease in catalyst activity.

With the exception of the discontinuous surface and the presence of obstacles imposed by the presence of micropores, the results are in agreement with the proposition of Iler [36], in which he considers that, in small pore diameters, the dehydroxilation reactions are hindered. In this case, a higher density of vicinal silanol groups would promote the generation of bidentate or even bimolecular species, which are known to be inactive for olefin polymerization. In order to attempt the detection of such species in the supports bearing a pore diameter lower than 100 Å, the samples were analyzed by MALDI-TOF-MS. Fig. 6 shows mass spectra of positive ions of HYD and G56 catalysts.

The HYD catalyst presents a mean pore diameter of 39 Å, while for G56 it is 145 Å. In both cases $[SiOH]^+$ ions with m/z of 45 are present, suggesting the presence of SiO moieties and of residual

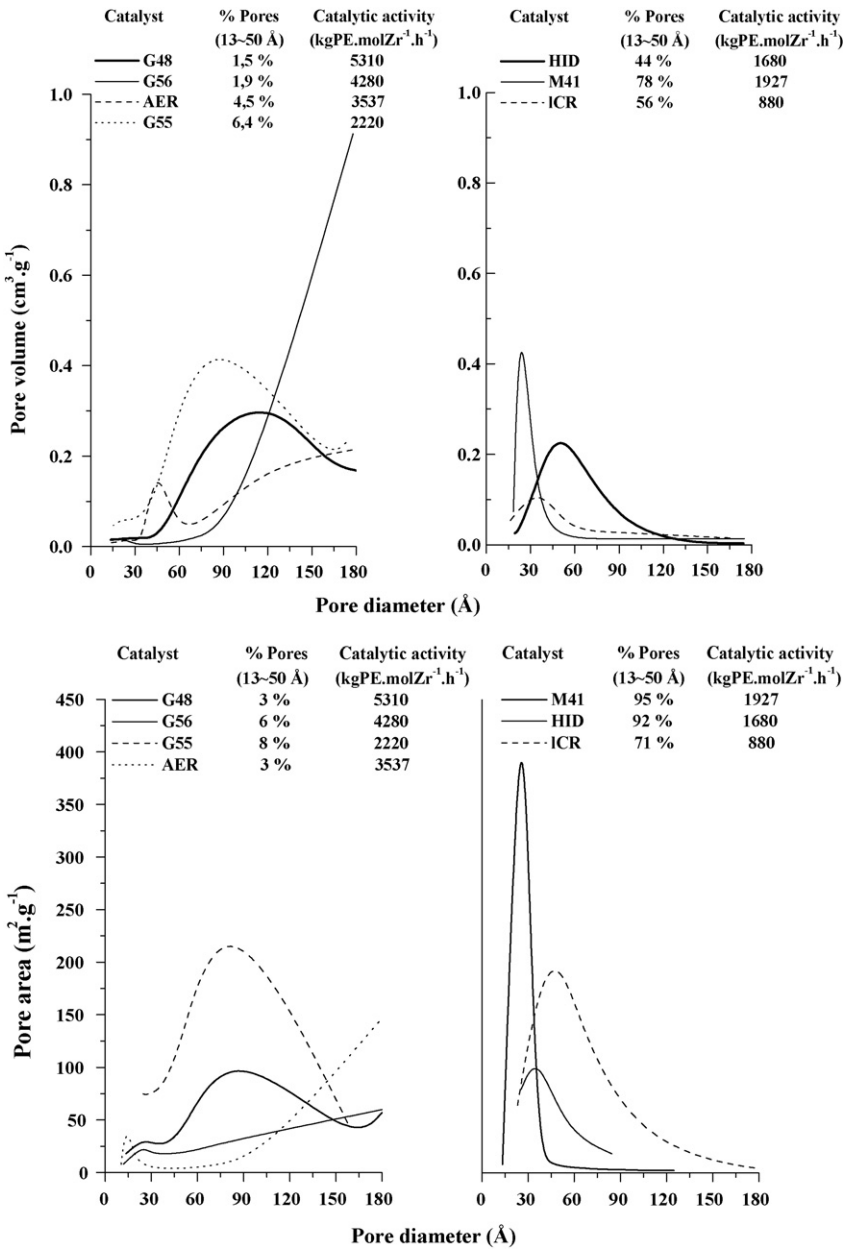

Fig. 5. Mean pore size distribution curves of the supported catalysts in terms of pore mean volume (top) and pore mean area (bottom).

silanol groups on the surface. For both catalysts, peaks at 91 *m*/*z* indicate the presence of Zr, while fragments at 128 *m*/*z* indicate the presence of $ZrCl^+$ species. For G56, the spectrum shows peaks at 229, 264, 308, 394 and 423 *m*/*z*, associated with fragments of the monometallic form. For signals higher than 423 *m*/*z*, a sequence of peaks of low intensity are assignable to fragments bearing SiO moieties. In the case of the HYD catalyst, a peak at 301 *m*/*z* can be attributed to the [*n*BuCpZrOSiOSi] fragment. For values higher than 421 *m*/*z*, the peaks suggest the existence of fragments associated with bimolecular metallocene species, such as those attributed to the peaks at 421, 437, 515, 541 and 715 *m*/*z* in Fig. 6. Peaks of low intensity, bearing a difference of 17 *m*/*z* suggest fragments involving OH groups. Such peaks are more abundant in the mass spectrum of HID.

The large number of bimolecular species in the mass spectrum of HYD is in agreement with the hypothesis that, in pores with narrower diameter (<100 Å), the proximity among intra-globular silanol groups would facilitate the generation of bimolecular species, as depicted in Scheme 2.

It is worth noting that according to MALDI-TOF-MS spectra, bimolecular species originating from the association of two molecules of Cp_2ZrCl_2 or one molecule of Cp_2ZrCl_2 and another of $(n\text{BuCp})_2ZrCl_2$ could be observed. Nevertheless, species originating from the combination of two $(n\text{BuCp})_2ZrCl_2$ could not be detected, probably due to steric effects caused by the *n*Bu ligands attached to the Cp rings.

As shown in Fig. 5, the distribution of the pore size of the supports suggests an effect of the surface relief on the catalyst activity. As previously discussed, a larger fraction of pores of smaller diameter (<100 Å) engenders diffusional restrictions to the monomer and cocatalyst due to the potential presence of obstacles on the surface. In this case, a large fraction of obstacles implies a higher surface roughness. AFM is a technique, complementary to nitrogen adsorption, which aids in the characterization of micro- and mesoporous

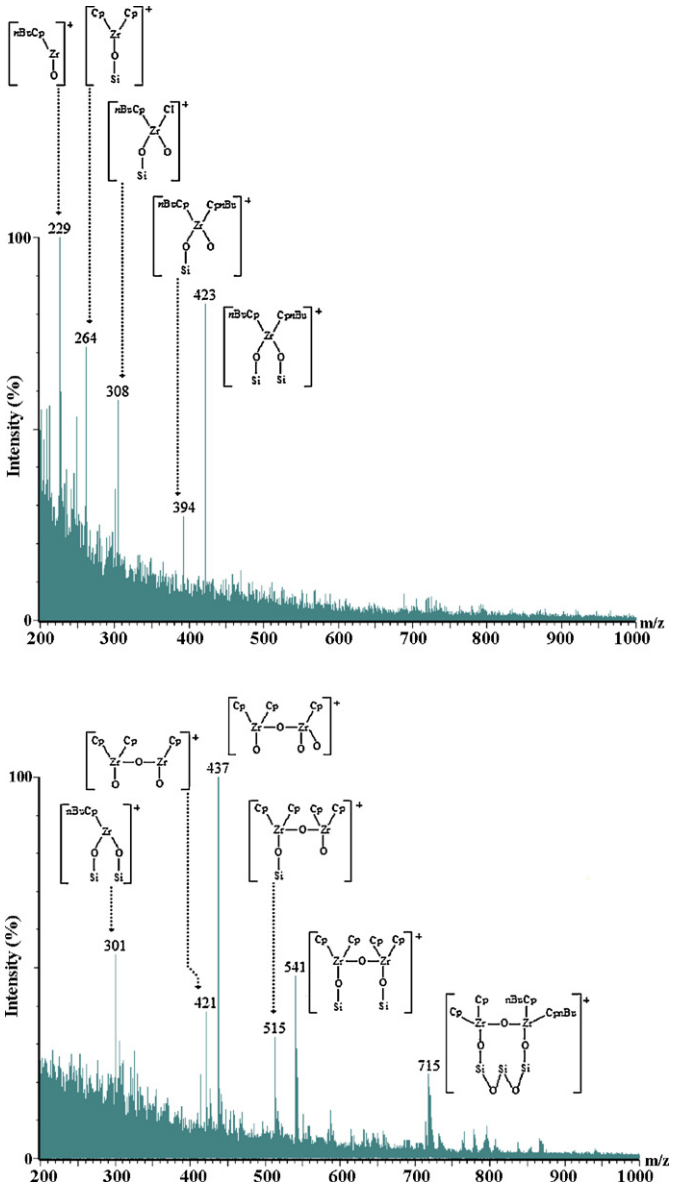

Fig. 6. MALDI-TOF-MS spectra of positive ions (m/z 0–1000) for G56 (top) and HYD (bottom).

surfaces [43]. In the case of supported catalysts, AFM images (Fig. 7) complement the results obtained by the BET method, by providing images of the type of relief (slits, holes and particle morphology).

For the supported catalysts employing commercial silicas (G48 and G55), the AFM images show homogeneity both in grain and pore shape (Fig. 7). The mesopores of such systems present slits between compact grains with a pore diameter in the range of 130 Å, in agreement with data obtained by the BET method (see Table 1). In the case of lCR, whose support is characterized by a fiber-like silica, a certain degree of regularity can be observed in the size of the layers that constitute the grain.

The AFM technique provides information for the determination of the root mean square (RMS) roughness of the surface of the catalyst particles, as shown in Fig. 8.

The RMS roughness of the catalyst surface is in agreement with the observed trend in the case of small pore content, which was associated with obstacles on the surface. In other words, as surface roughness (obstacles) increases, the catalyst activity in ethylene polymerization decreases.

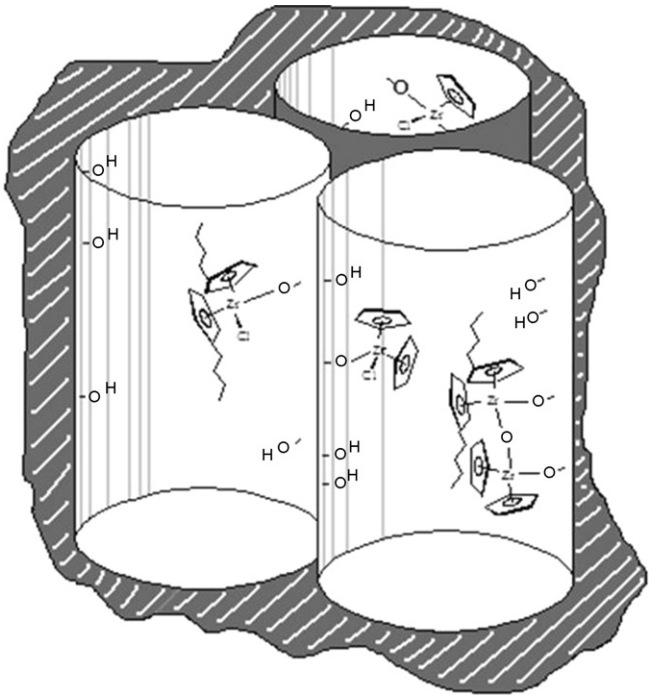

Scheme 2. Effect of the narrow pore diameter on the nature of the generated supported metallocene species.

3.2. Polymer characteristics

The resulting polymers were characterized by GPC and DSC. Table 3 shows data concerning polymer molecular weight, polydispersity index (PDI) and crystallinity (χ_c).

According to Table 3, the polymer molecular weight was shown to be between 258 and 484 kg mol^{-1}. The PDI remained around 2. The largest broadening was observed in the case of polyethylene produced by HID.

The polymers presented similar melting points (around 133 °C), and the crystallinity lain in the range of 31–66%. In the case of polymers produced with supported catalysts based on commercial silicas, an increase in molecular weight was accompanied with an increase in crystallinity.

The M41 catalyst system produced polymers with intermediary molecular weight in comparison to those data reported in the literature. For instance, Rahiala et al. [44] obtained a polymer of 431 kg mol^{-1} using Cp_2ZrCl_2/MCM-41 at polymerization conditions of 50 °C and 2.5 bar. In the case of (nBuCp)$_2$ZrCl$_2$/MCM-41, Kumkaew et al. [45] obtained polymers with lower molecular weights (260 kg mol^{-1}) using gas-phase ethylene polymerization. Dong et al. [46] immobilized Cp_2ZrCl_2 within MCM-41 pores and proposed an extrusion mechanism in which the polymer

Table 3
Polymer properties of the resulting polyethylenes.

Catalyst	Molecular weight (kg mol^{-1})	PDI	χ_c (%)
G56	423	2.0	66.0
G55	338	2.1	49.8
G48	258	1.9	60.4
HYD	356	3.0	47.4
AER	343	2.0	53.0
ICR	484	1.9	31.0
M41	378	2.1	49.0

[Zr] = 10^{-5} mol L^{-1}; [Al/Zr] = 1000; V = 0.15 L toluene; P = 1 bar ethylene; T = 60 °C; t = 30 min.

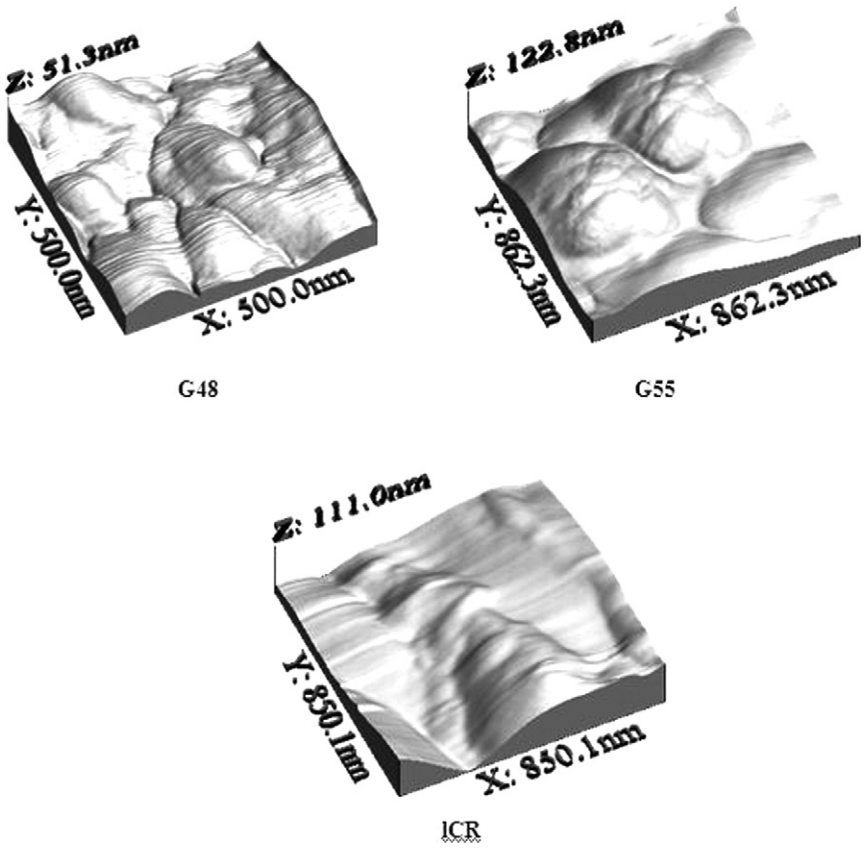

Fig. 7. AFM images of G48, G55 and ICR samples.

chains are oriented by the support pores generating polymers nano-fibers.

Fig. 9 shows the XRD patterns of the polyethylene samples prepared with G48, ICR and M41. The orthorhombic crystalline fraction of polyethylene present in the samples corresponds to diffraction peaks at 21.6° and 24° (G48 and M41), and 21.8° and 24° (ICR), suggesting the existence of extended-chain crystals [46,47]. The lower diffraction intensity in the case of polyethylene produced by ICR is in agreement with the lower crystallinity determined for this polymer (χ = 31%). The small *halo* around 19.5° indicates the existence of folded-chains.

The morphologies of the resulting polymers were studied by SEM. Fig. 10 shows the SEM micrographs of polymers obtained with catalysts G48, ICR and M41, revealing the existence of fibers.

The polymer obtained with catalyst G48 presents nano-fibers with 20.5 nm size, calculated from the signal full width at half maximum (FHWM). The polymer produced by M41 presents fibers with 102 width, and nano-fibers with 12.5 nm. For the polymer

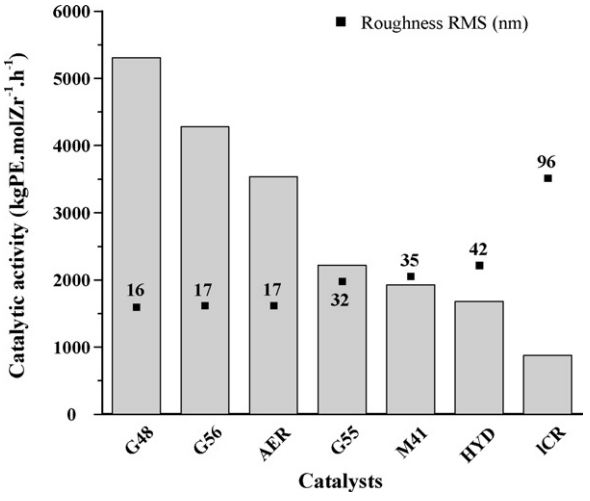

Fig. 8. Effect of the surface RMS roughness of the supported catalysts, determined by AFM, on the catalytic activity in ethylene polymerization.

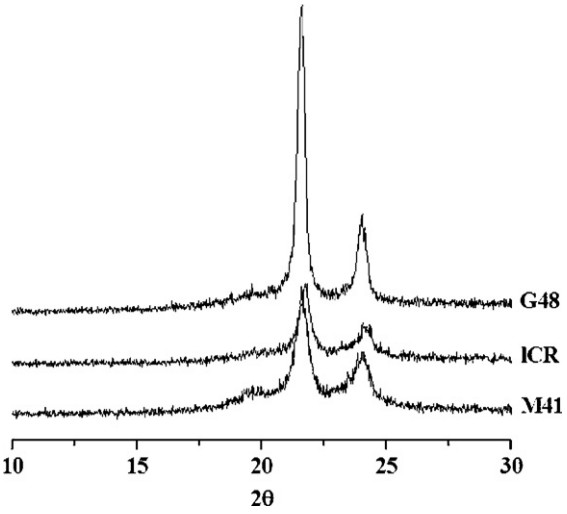

Fig. 9. XRD patterns of PE obtained with G48, ICR and M41 supported catalysts.

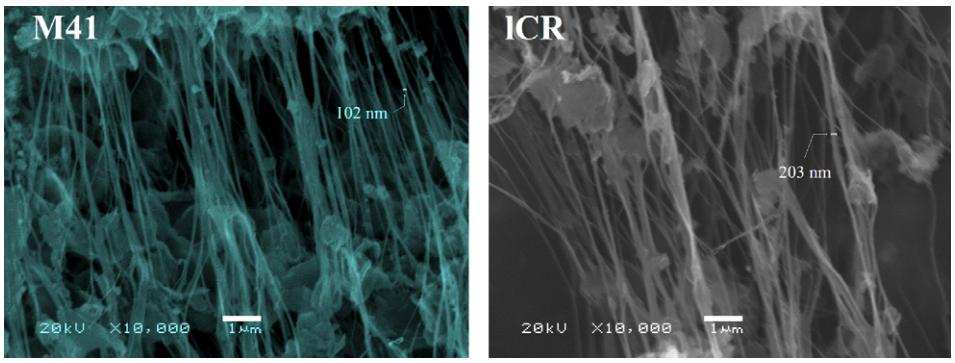

Fig. 10. SEM micrographs of polymers fibers obtained with supported catalysts M41 and lCR.

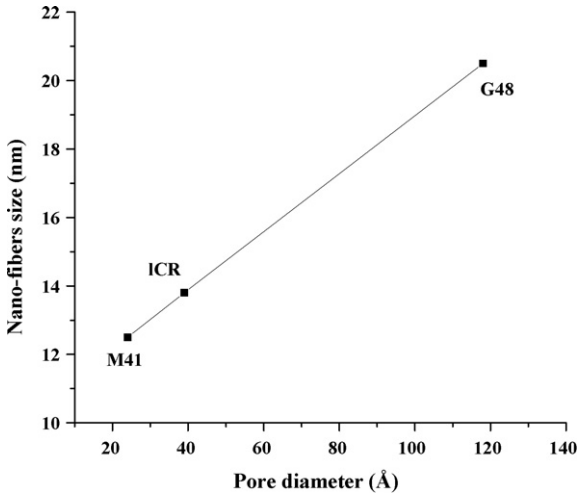

Fig. 11. Relationship between the support pore diameter and the size of the fibers of the resulting polymers.

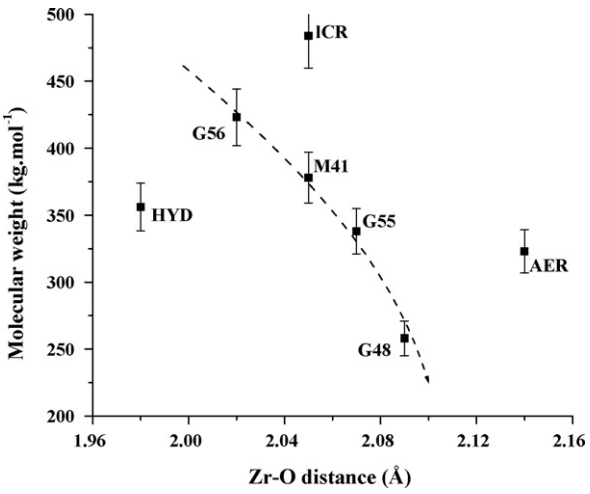

Fig. 12. Effect of the Zr–O distance on the molecular weight of the resulting polymers.

produced by the catalyst support on chrysotile, the fibers presented 203 nm width and the nano-fiber in the range of 13.8 nm size. Fig. 11 shows the relationship between support pore diameter of the catalyst and the size of the nano-fibers present in the polymeric material.

As the pore size increases, the monomer diffusion to the catalyst sites is favored, facilitating the growth of the polymer chain. Supports with smaller pore diameter seem to control the direction of chain propagation, forming extended chains.

Fig. 12 shows the relationship between the Zr–O interatomic distance and polymer molecular weight, suggesting that the support, or the structure of the grafted species, can influence the molecular weight of the produced polymer.

Among catalyst systems using commercial silica as a support, G48 generated the polymer of the lowest molecular weight, as shown in Fig. 12. As already reported in literature [37], blocking one of the sides of the catalytic site on the support slows the termination step due to steric effects on the surface, which acts as a ligand. In other words, the chain transfer reaction by β-elimination

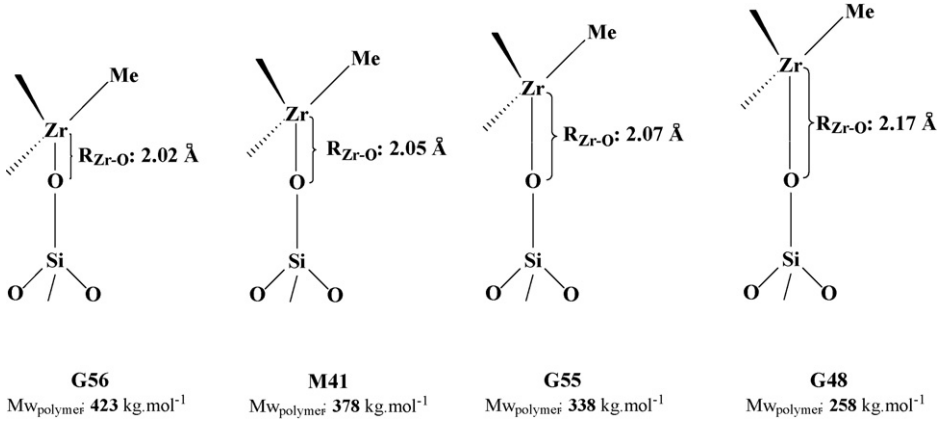

Scheme 3. Effect of the interatomic Zr–O bond distance (R_{Zr-O}) on the molecular weight of the resulting polymers.

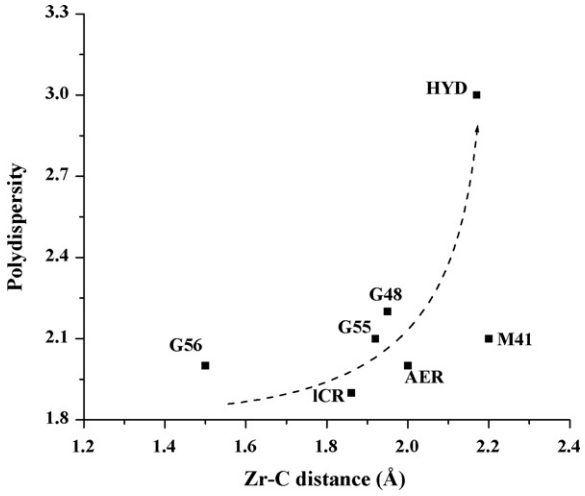

Fig. 13. Influence of the Zr–C distance on the polydispersity of the resulting polymers.

is hindered, affording an enhancement in the growth of the polymer chain, increasing the molecular weight [48]. In the case of G48, G55, G56 and M41, EXAFS and GPC measurements suggests that the longer Zr–O distance, in the case of G48, render it less sterically hindered, which in turn might favor chain termination reactions, producing a polymer with lower molecular weight in comparison to those produced by G55, G56 or M41. In such systems, as the Zr–O distance decreases, the molecular weight of the produced polymer decreases, as depicted in Scheme 3.

For HID, ICR and AER supported catalysts, no clear relationship between Zr–O bond and molecular weight could be deduced.

Regarding polydispersity, Fig. 13 shows that an increase in the Zr–C bond distance of the supported metallocene causes broadening in the molecular weight distribution of the resulting polymers.

The trend observed in Fig. 13 suggests that a longer Zr–C distance might engender the formation of catalyst systems that are more prone to olefin insertion errors and/or termination reactions, which in turn might affect the total distribution of the produced molecular weight. Burger et al. [49] studied the steric effect caused by the metallocene structure and its influence on the properties of the resulting polymer by affecting olefin insertion errors and polymer chain termination reactions. Thus, the increase in the mean Zr–C interatomic distance in the metallocene-supported species may favor the production of polymers with a small bias in molecular weight, broadening the polydispersity.

4. Conclusions

The textural properties of the silica support were shown to influence several parameters and properties of supported metallocene catalysts. The pore diameter and pore size distribution influence the catalyst activity and the structure of the supported metallocene. Silicas with narrower pore diameters presented lower catalyst activities probably due to the higher probability of formation of bimolecular species, which are inactive to olefin polymerization. The large fraction of pores with small diameter also contribute to the formation of surface obstacles, which might hinder reactant diffusion.

The molecular weight of the obtained polymers seems to be strongly influenced by the structure of the immobilized metallocene, depending on the distance between the metallic center and the surface of the support. The polydispersity also seems to be affected by the distance between the metallic center and the ligands, which might induce olefin misinsertion during the polymer chain growth engendering polydispersity broadening. Furthermore, the morphology of the polymers may be induced by the textural properties of the support.

Acknowledgements

This work was partially financed by CNPq and FAPERGS/PRONEX. The authors are thankful to LNLS for measurements in the EXAFS beamline (Project D04B XAFS1#5839) and for MALDI-TOF-MS (Project MAS#6406). Mr. William Bretas Linares from SAMA is specially thanked for providing chrysotile samples. We thank Braskem for GPC analysis.

References

[1] J.R. Severn, J.C. Chadwick, R. Duchateau, N. Friederichs, Chem. Rev. 105 (2005) 4073.
[2] M.R. Ribeiro, A. Deffieux, M.F. Portela, Ind. Eng. Chem. Res. 36 (1997) 1224.
[3] R. Guimarães, F.C. Stedile, J.H.Z. dos Santos, J. Mol. Catal. A: Chem. 206 (2003) 353.
[4] H. Hammawa, S.E. Wanke, J. Appl. Polym. Sci. 104 (2007) 514.
[5] M.W. McKittrici, C.W. Jones, Chem. Mater. 17 (2005) 4758.
[6] R.M. Kasi, E.B. Coughlin, Organometallics 22 (2003) 1534.
[7] L. Burkett, S. Soukasene, K.L. Milton, R. Welch, A.J. Little, R.M. Kasi, E.B. Coughlin, Chem. Mater. 17 (2005) 2716.
[8] D. Bianchini, K.M. Bichinho, J.H.Z. dos Santos, Polymer 43 (2002) 2937.
[9] J.P.J. Turunen, T. Venäläinen, S. Suvanto, T.T. Pakkanen, J. Polym. Sci. Part A: Polym. Chem. 45 (2007) 4002.
[10] C.S. Reddy, C.K. Das, J. Polym. Res. 14 (2007) 129.
[11] R. Van Grieken, A. Carrero, I. Suarez, B. Paredes, Eur. Polym. J. 43 (2007) 1267.
[12] A.S. Shearer, Y.R. De Miguel, E.A. Munich, D. Pochan, C. Jenny, Inorg. Chem. Commun. 10 (2007) 262.
[13] A.G. Fisch, N.S.M. Cardozo, A.R. Secchi, F.C. Stedile, N.P. da Silveira, J.H.Z. dos Santos, J. Non-Crystal. Solids 354 (2008) 3973–3979.
[14] J.C. Hicks, B.A. Mullis, C.W. Jones, J. Am. Chem. Soc. 129 (2007) 8426.
[15] R. Huang, R. Duchateau, C.E. Koning, J.C. Chadwick, Macromolecules 41 (2008) 579–590.
[16] F. Silveira, S.R. Loureiro, G.B. Galland, F.C. Stedile, J.H.Z. dos Santos, T. Teranishi, J. Mol. Catal. A: Chem. 206 (2003) 389–398.
[17] S.R. Rodrigues, F. Silveira, J.H.Z. dos Santos, M.L. Ferreira, J. Mol. Catal. A: Chem. 216 (2004) 19–27.
[18] F. Silveira, G.P. Pires, C.F. Petry, D. Pozebon, F.C. Stedile, J.H.Z. dos Santos, A. Rigacci, J. Mol. Catal. A: Chem. 265 (2007) 167–176.
[19] T. Kawaguchi, K. Ono, J. Non-Cryst. Solids 121 (1990) 383–388.
[20] B. Karmakar, G. De, D. Ganguli, J. Non-Cryst. Solids 272 (2000) 119–126.
[21] A. Rigacci, F.E. -Dolle, E. Geissler, B. Chevalier, H. Sallée, P. Achard, O. Barbieri, S. Berthon, F. Bley, F. Livet, G.M. Pajonk, N. Pinto, C. Rochas, J. Non-Cryst. Solids 285 (2001) 187–193.
[22] M.G. Fonseca, A.S. Oliveira, C. Airoldi, J. Colloidal Interface Sci. 240 (2001) 533–538.
[23] F.C. Stedile, J.H.Z. dos Santos, Phys. Stat. Sol. 173 (1999) 123–134.
[24] I. Horcas, R. Fernandez, J.M. Gomez-Rodriguez, J. Colchero, J. Gomez-Herrero, A.M. Baro, Rev. Sci. Instrum. 78 (2007) 013705.
[25] T. Ressler, J. Synch. Rad. 5 (1998) 118–122.
[26] J.J. Rehr, R.C. Albers, Rev. Mod. Phys. 72 (2000) 621–654.
[27] B. Ravel, J. Synchrotron Rad. 8 (2001) 314–316.
[28] R.E. Duderstadt, B.M. Tsuie, S.F. Macha, P.A. Limbach, Anal. Chim. Acta 596 (2007) 124–131.
[29] V. Volkis, A. Lisovskii, B. Tumanskii, M. Shuster, M.S. Eisen, Organometallics 25 (2006) 2656–2666.
[30] A. Morow, Stud. Surf. Sci. Catal. 57 (1990) 161–224.
[31] U. Schubert, N. Hüsing, Angew. Chem. Int. Ed. 37 (1998) 23–45.
[32] A. Stein, B.J. Melde, R.C. Schroden, Adv. Mater. 12 (2000) 1403–1419.
[33] L. Wang, C. Lu, X. Li, X. Zheng, D. Zhao, R. Liu, Ac. Geo. Sin. 80 (2006) 180–189.
[34] N. Mäkelä-Vaarne, D.G. Nicholson, A.L. Ramstad, J. Mol. Catal. A: Chem. 200 (2003) 323–332.
[35] M. Jezequel, V. Dufaud, M.J. Ruiz-Garcia, F. Carrillo-Hermosilla, U. Neugebauer, G. Niccolai, F. Lefebvre, F. Bayard, J. Corker, S. Fiddy, J. Evans, J.-P. Broyer, J. Malinge, J.-M. Basset, J. Mol. Catal. A: Chem. 123 (2001) 3520–3540.
[36] R.K. Iler, Chemistry of Silica, Willey, New York, 1979.
[37] J.H.Z. dos Santos, C. Krug, M.B. da Rosa, F.C. Stedile, J. Dupont, M.M.C. Forte, J. Mol. Catal. Chem. 139 (1999) 199–207.
[38] A.P. Legrand, H. Hommel, A. Tuel, A. Vidal, H. Balard, E. Papirer, P. Levitz, M. Czernichowski, R. Erre, H. Van Damme, J.P. Gallas, J.F. Hemidy, J.C. Lavalley, O. Barres, A. Burneau, Y. Grillet, Adv. Colloid Interface Sci. 33 (1990) 91–330.

[39] T.J. Pullukat, in: M. Terano, T. Shiono (Eds.), Future Technology for Polyolefin and Olefin Polymerization Catalysis, Technology and Education Publishers, Tokyo, 2002, pp. 147–155.
[40] B.M. Weckhuysen, R.A. Schoonheydt, Catal. Today 51 (1999) 215–221.
[41] M.P. McDaniel, Adv. Catal. 33 (1985) 47–98.
[42] D. Stoiljkovic, B. Pilic, M. Bulajic, N. Durasovic, N. Ostrovskii, J. Serb. Chem. Soc. 73 (2008) 97–111.
[43] J.I. Paredes, A. Martínez-Alonso, J.M.D. Tascón, Microporous Mesoporous Mater. 65 (2003) 93–126.
[44] H. Rahiala, I. Beurroies, T. Eklund, K. Hakala, R. Gougeon, P. Trens, J.B. Rosenholm, J. Catal. 188 (1999) 14–23.
[45] P. Kumkaew, S.E. Wanke, P. Praserthdam, C. Danumah, S. Kaliaguine, J. Appl. Polym. Sci. 87 (2003) 1161–1177.
[46] X. Dong, L. Wang, W. Wang, H. Yu, J. Wang, T. Chen, Z. Zhao, Eur. Polym. J. 41 (2005) 797–803.
[47] Z.B. Ye, S.P. Zhu, W.J. Wang, H. Alsyouri, Y.S. Lin, J. Polym. Sci., Part B: Polym. Phys. 41 (2003) 2433–2443.
[48] W. Kaminsky, F. Renner, Makromol. Chem. Rapid Commun. 14 (1993) 239–243.
[49] P. Burger, K. Hortmann, H.-H. Brintzinger, Makromol. Chem., Macromol. Symp. 66 (1993) 127–139.